

A simulation package — SASAL for X-ray and EUV spectroscopy of astrophysical and laboratory plasmas *

Gui-Yun Liang¹, Fang Li¹, Fei-Lu Wang¹, Yong Wu², Jia-Yong Zhong¹ and Gang Zhao¹

¹ Key Laboratory of Optical Astronomy, National Astronomical Observatories, Chinese Academy of Sciences, Beijing 100012, China; gyliang@bao.ac.cn

² Data Center for High Energy Density Physics, Institute of Applied Physics and Computational Mathematics, Beijing 100088, China

Received 2013 September 24; accepted 2014 April 1

Abstract For the laboratory astrophysics community, those spectroscopic modeling codes extensively used in astronomy, e.g. Chianti, AtomDB, Cloudy and Xstar, cannot be directly applied to analyzing laboratory measurements due to their discrepancies from astrophysical cases. For example, plasma from an electron beam ion trap has an electron energy distribution that follows a Gaussian profile, instead of a Maxwellian one. The laboratory miniature for a compact object produced by a laser-driven implosion shows a departure from equilibrium, that often occurs in celestial objects, so we setup a spectral analysis system for astrophysical and laboratory (SASAL) plasmas to act as a bridge between them, which benefits the laboratory astrophysical community.

Key words: atomic data — line: formation — plasmas — X-rays: general

1 INTRODUCTION

In X-ray and extreme ultraviolet astronomy, there are several spectral modeling codes that help us understand the observational data for various objects. For example, the work by Chianti (Landi et al. 2012a) is extensively used by the solar physics community to analyze various spectroscopic (i.e. *Hinode*¹) and imaging (*Solar Dynamics Observatory*, *SDO*²) data observed by many space missions. The MEKAL (Mewe et al. 1995) and AtomDB (Smith et al. 2001) models focus on spectroscopy in the X-ray region for various X-ray emitters. Cloudy (Ferland et al. 1998) and Xstar (Kallman & Bautista 2001) are the dominant models used for analysis of photoionized astrophysical plasmas, e.g. warm absorber (Ashton 1993) and stellar winds from a Wolf-Rayet companion star (Paerels et al. 2000). However, all these models strongly depend on the accuracy of data generated by underlying atomic processes. A different branch of astrophysical research – Laboratory Astrophysics – appears to benchmark the theoretical models of celestial emissions (Foord et al. 2004; Fournier et al. 2001).

However, with presently used techniques, laboratory plasmas cannot achieve the same conditions as those appearing in the distant Universe. For example, an electron beam ion trap (EBIT) has

* Supported by the National Natural Science Foundation of China.

¹ <http://solarb.msfc.nasa.gov/>

² <http://sdo.gsfc.nasa.gov/>

often been used to benchmark various spectral models for plasmas that arise from electron collisions or to help line identification for a coronal-like plasma due to its consistent plasma conditions (via the electron density ranging between 10^9 – 10^{13} cm^{-3}) to astrophysical cases (Liang et al. 2009). Moreover, various atomic processes for line emissions can be dissociated in this facility. Yet, EBIT generally uses monoenergetic electron beams, which differ from the thermal electrons in most astrophysical phenomena. This platform is further used to simulate X-ray emissions produced by charge exchange in comets (Beiersdorfer et al. 2003). However, the kinetic energy (with velocity that is tens of km s^{-1}) of trapped ions is lower than that of the solar wind by an order of magnitude, wherever the solar wind velocity has been theoretically confirmed to be important for line emissions (Bodewits et al. 2007).

Recently, other laboratory platforms were used to model conditions around objects like a black hole, such as Z-pinch and an intense laser (Fujioka et al. 2009). Moreover, laboratory miniatures have a strong gradient in temperature and density, and have an extremely short lifetime of tens to hundreds of picoseconds to a nanosecond. Usually, the laboratory plasmas deviate from ionization equilibrium. By contrast, the gradient of plasma conditions (electron density and/or temperature) and the lifetimes of astrophysical plasmas are negligible and long, respectively. So, a complete, self-consistent model is necessary to act as a bridge between laboratory and astrophysical plasmas.

In this work, we present details about the technique used in an analysis package – the Spectral Analysis System for Astrophysical and Laboratory plasmas (SASAL). The physical details are presented in paper I (Liang et al. 2014). A brief description of the spectroscopic model and atomic data are outlined in Section 2. Section 3 illustrates modules for the spectroscopy of an electron collision with thermal and monoenergetic (e.g. EBIT case) electrons, photoionization and charge-exchange heating and/or cooling mechanisms. Non-equilibrium effects on the spectroscopy and charge state distribution are implemented in the present model with the inclusion of a metastable contribution. Some applications are also presented in this section. The last section outlines a summary.

2 SASAL MODEL AND ATOMIC DATA

The SASAL model consists of two modules – ionization equilibrium and non-equilibrium cases, as shown in Figure 1. With regard to the plasma heating mechanism, various astrophysical and laboratory plasmas contain electron collision, photoionization and charge-exchange processes, so SASAL is further divided into three components for ionization equilibrium and non-equilibrium spectroscopy, respectively, as well as a module for charge state distribution for those three kinds of plasmas in ionization equilibrium and non-equilibrium states. As shown in Figure 1, various atomic processes represent fundamental physics in the SASAL model, including structure data (i.e. energy level and radiative decay rates), excitation data (for electron, proton and photon collision), total and level resolved collisional ionization, photoionization and dielectronic/radiative recombination, as well as charge-exchange data. By including the level-resolved ionization and recombination data, the SASAL model can be used to investigate the effect of a metastable population on spectroscopy and charge state distribution.

Figure 2 shows the main menu for the SASAL package. By selecting a given item, users can setup a graphical interface for X-ray and EUV spectroscopy that can be applied to different kinds of plasmas. The details will be presented in the following sections.

In this package, the assumption of being optically thin is adopted. Populations of a particular ionic species at a given level (X^{q+}) include contributions from electron/proton/photon impact (de-)excitation, electron/photon collision ionization (CI) from a lower neighboring ion (X^{q-1}), dielectronic/radiative recombination (DR/RR) from a higher neighboring ion (X^{q+1}), charge transfer in collisions with neutral atoms and molecules, and subsequent radiative decays, either directly to the ground and lower excited states or via cascades.

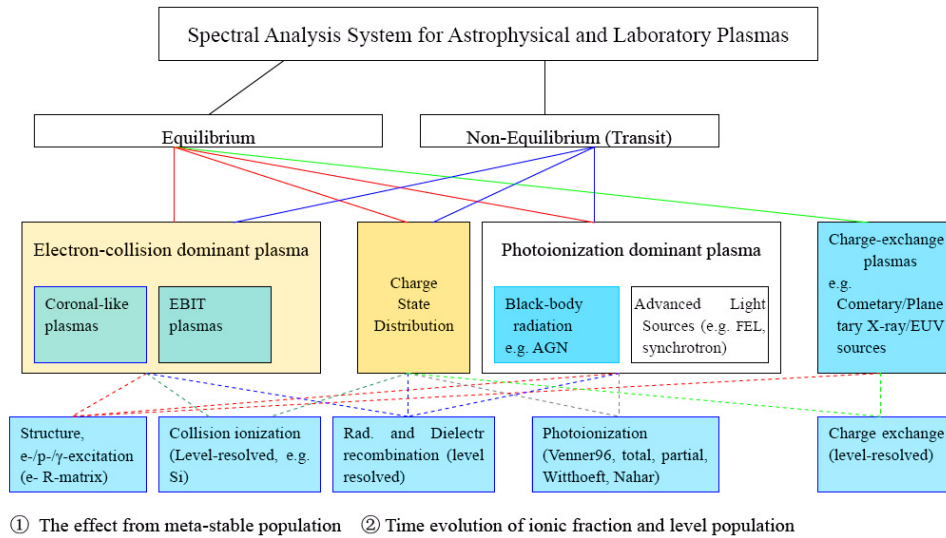


Fig. 1 A schematic of the SASAL spectroscopic modeling codes. Metastable contributions (marked by ①) from and/or to populations of neighboring ions at a given level and ionic fraction are included, in addition to their time dependence (marked by ②).

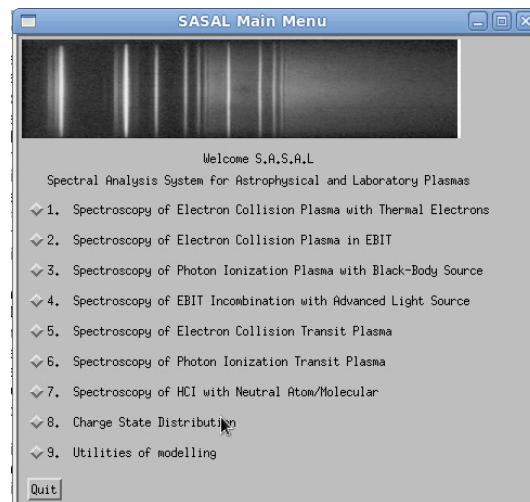


Fig. 2 The main menu of the SASAL package. It consists of nine spectroscopic modeling functions for electron collisional plasmas with thermal electrons (1) and non-thermal electrons (2– monoenergetic electron beams), photoionized plasmas with a black body radiation source (3) and advanced light source (4, i.e. free electron laser source), non-equilibrium collisional (5) and photoionized plasmas (6), charge-exchange emissions as in solar wind interaction with neutral atoms and molecules (7), and the charge state distribution in equilibrium and non-equilibrium plasma for different plasmas (8), as well as their utilities (9).

These transitions are described by the following equation:

$$\frac{d}{dt}n_i^{q+} = n_e \sum_{j \neq i} n_j^{q+} (Q_{ji}(T_e) + P_{ji}(T_e)) + \sum_{j > i} n_j^{q+} A_{ji} \quad (1)$$

$$-n_i^{q+} \left[n_e \sum_{j \neq i} (Q_{ij}(T_e) + P_{ij}(T_e)) + \sum_{i < j} A_{ij} \right] \quad (2)$$

$$+n_e \left[\sum_{i'=0}^{m^{q-1}} n_{i'}^{(q-1)+} S_{i'i}(T_e) + \sum_{j'=0}^{m^{q+1}} n_{j'}^{(q+1)+} \alpha_{j'i}(T_e) \right] \quad (3)$$

$$-n_e \left[\sum_{i'} n_i^{q+} S_{i'i'}(T_e) + \sum_{j'} n_i^{q+} \alpha_{ij'}(T_e) \right] \quad (4)$$

$$+\gamma \left[\sum_{i'} n_{i'}^{(q-1)+} \theta_{i'i}(E) - \sum_{j'} n_i^{q+} \theta_{ij'}(E) \right] \quad (5)$$

$$+n_{\text{mol}} \left[\sum_{i'} n_{i'}^{(q+1)+} C_{i'i}(T_e) - \sum_{j'} n_i^{q+} C_{ij'} \right], \quad (6)$$

where n_i^{q+} is the number density of $q+$ charged ions in the i^{th} state, while n_e , γ and n_{mol} correspond to the number density of electrons, photons and neutral atoms/molecules, respectively. Q_{ij} refers to the rate coefficient for electron/proton impact (de-)excitation, P_{ij} corresponds to the rate coefficient for photon (de-)excitation, rate coefficients $S_{i'i}$ and $\alpha_{j'i}$ correspond to ionization from electron impact and dielectronic plus radiative recombination, respectively. θ_{ij} and C_{ij} are rate coefficients for photoionization and charge-exchange recombination, respectively. The first, second and third terms in the right part of the equation correspond to contributions from electron/proton excitations and subsequent radiative decays. The terms in (3) and (4) denote the contributions from electron impact ionization and dielectronic plus radiative recombination. The terms in (5) and (6) refer to population and depopulation due to photoionization (PI) and charge-exchange from neighboring ions. The above complex equation can be simplified to be

$$d \frac{\vec{N}}{dt} = \mathbf{A} \vec{N} \quad (7)$$

where \mathbf{A} is a stiffness matrix consisting of parameters of various atomic processes mentioned above, and \vec{N} refers to a scalar consisting of populations at levels $\{n_1, n_2, n_3, \dots, n_{\text{max}}\}$.

The present SASAL package not only allows access to the Chianti database (Landi et al. 2012a, v7), but also implements pipeline access by many IDL codes to those data under the UK Rmax and APAP network³, and to those performed by Witthoef and co-authors (2009, 2011a,b), as well as to data⁴ calculated by Nahar and coauthors (2000). These include data about atomic structure, electron impact excitation (Liang et al. 2012, and references therein), photoionization, and dielectronic and radiative recombination (Badnell et al. 2003; Badnell 2006). Level-resolved collisional ionizations with/without excitation autoionization can be done automatically in SASAL with pre-defined atomic models by using AUTOSTRUCTURE (Badnell 1986) and/or flexible atomic code (FAC, Gu 2008) methods for K-shell and L-shell ions. For those M-shell ions, the Chianti v7 compilation is adopted.

³ <http://www.apap-network.org>

⁴ <http://www.astronomy.ohio-state.edu/~nahar/>

Compilations of earlier fits performed by Venner et al. (1996) for photoionization are included by a modified ‘phfit.f’ program. For the excitation data, He-like, Li-like, B-like, F-like, Ne-like and Na-like isoelectronic sequences from singly ionized cases through krypton–Kr ($Z = 36$) have been included (Liang et al. 2012, and references therein), where the intermediate coupling framework transformation (ICFT) R -matrix method has been adopted for the excitations. For dielectronic and radiative recombination data, K-shell, L-shell, Na-like, Mg-like and Al-like iso-electronic sequences for ions from H through Zn^5 have been incorporated into the present model, including analytical fits for metastable levels and partially level-resolved recombination rates. The validity of the analytical formula has been examined by Gao & Zeng (2010). Moreover, online calculations for energy levels, radiative decay rates, autoionizations and electron impact excitations have been incorporated into the SASAL model by using AUTOSTRUCTURE and/or FAC methods. Furthermore, online calculation for the charge-exchange (CX) cross section by using the method described by multichannel Landau-Zener theory with rotational coupling (MCLZRC, Janev et al. 1983; Butler & Dalgarno 1980) has been implemented in the present model, in addition to collections of CX cross section data from methods using atomic-orbital close-coupling and/or molecular-orbital close-coupling (Wu et al. 2011). Such an *ab initio* quantum mechanical approach is usually regarded as more accurate at incident energies below a few hundred eV per nucleus. The resultant LS -manifold cross sections are distributed into J -levels according to the relative statistical weight of each level. Additionally, we complement the hydrogenic model that is adopted by Wegmann et al. (1998) into the present spectroscopic model to estimate the CX cross sections as done by Smith et al. (2012), that is,

$$\sigma = 8.8 \times 10^{-17} \left(\frac{q-1}{q^2/2n^2 - |I_p|} \right)^2, \quad (8)$$

where q is the charge of the projectile ion, n the principal quantum number of the captured ion with a peak in the distribution at $n = q\sqrt{\frac{1}{2|I_p|}} \left(1 + \frac{q-1}{\sqrt{2}q}\right)^{-1/2}$ and $|I_p|$ is the ionization potential of the target in atomic units (i.e., 1 a.u. = 27.2 eV). The n -manifold cross sections are distributed into l subshells according to the distribution function $W(l, n) = \frac{(2l+1)[(n-1)!]^2}{(n+l)!(n-l-1)!}$ for low $n \leq 8$ and $W(l, n) = \left(\frac{2l+1}{Z}\right)\exp\left(-\frac{l(l+1)}{Z}\right)$ for high $n > 8$ values (where Z is the nuclear charge). Finally, the level-resolved CX cross sections are obtained by the relative statistical weight of each level.

In the plasma generated by an EBIT, the electrons are unidirectional and quasi-monoenergetic with a small energy width. Line emissions from excited ions will be both anisotropic and polarized (Beiersdorfer et al. 1996; 1999). The linear polarization P at an observation angle $\vartheta = 90^\circ$ relative to the beam direction is given as $P = \frac{I_{\parallel} - I_{\perp}}{I_{\parallel} + I_{\perp}}$, where I_{\parallel} refers to the light intensity with the electric field vector parallel to the beam direction, and I_{\perp} corresponds to the light intensity with the electric field vector perpendicular to the beam direction. The observed line intensity has a relation with total line intensity I_{tot} in 4π steradians as $I_{\text{obs}} = \frac{3I_{\text{tot}}}{3-P}$. Polarization data files are compiled and incorporated in this model for some ions, e.g. highly charged iron ions in the work of Liang et al. (2009). However, only a small amount of data is available in the literature.

3 SPECTROSCOPIC MODULES FOR COLLISIONAL, PHOTOIONIZED AND CHARGE-EXCHANGE PLASMAS

3.1 ECPTE and ECP_EBIT Modules for Collisional Equilibrium Plasma

There are two modules for electron collisional plasma in the flowchart of Figure 3; one is for thermal electrons (ECPTE) and the other is for non-thermal (i.e. monoenergetic electron beam) electrons (ECP_EBIT).

⁵ <http://amdpp.phys.strath.ac.uk/tamoc/DATA/>

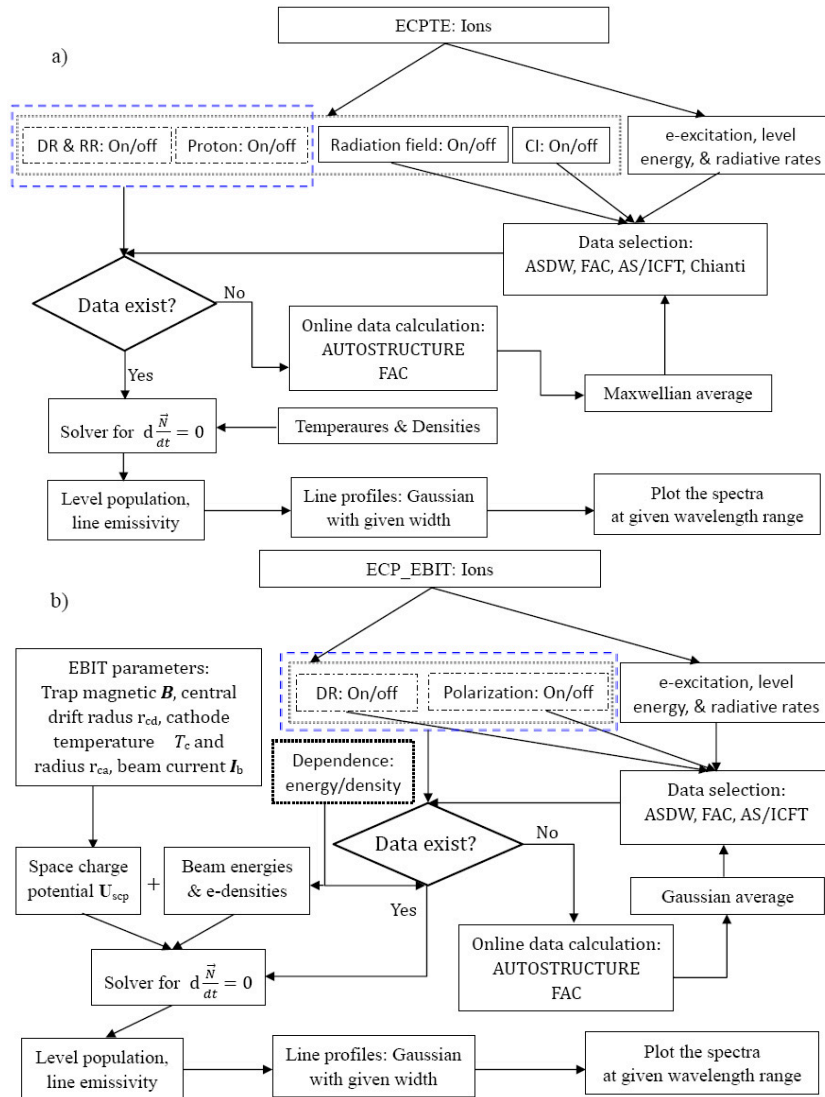


Fig. 3 Flowchart for the electron collisional spectroscopy with thermal (ECPTE) and monoenergetic (ECP.EBIT) electrons. Online calculations for energy levels, radiative decay rates and electron impact excitations by using AUTOSTRUCTURE and FAC codes have been implemented. Dotted-boxes denote that those processes that can be selected. The dashed box corresponds to the atomic data, which are compiled from the literature or public websites.

When an ion is selected, users can turn on/off the CI, DR/RR, proton impact excitation and photon (de-)excitation processes that are marked by the dotted boxes. However, the energy levels, radiative decay rates and excitations are necessary parameters for the ECPTE module, see Figure 3(a). The blue dashed box denotes that these two parameters for the two processes are the compiled data collected from published papers (Badnell et al. 2003; Badnell 2006) or websites³. As mentioned in the above section, the SASAL can access the Chianti (v7) database, and the data collected from

the UK APAP network³ (which mainly refers to data from the ICFT *R*-matrix calculation including excitations, and energy levels and radiative decay rates), as well as data from FAC and Breit-Pauli AUTOSTRUCTURE (ASDW) calculations. Users can select different data files for comparison. If there are no data available, the presented SASAL model will perform online FAC and ASDW calculations to obtain the necessary parameters, i.e. energy levels, radiative decay rates and collision cross sections. It also automatically performs a 12-point Gauss-Laguerre integration to obtain the effective collision strengths. By selecting the DR, RR and CI keywords, the ECPTTE module can be used to test the metastable contribution to spectroscopy from/to neighboring ions due to DR, RR and CI processes. Moreover, the present SASAL can perform online FAC and ASDW calculations to obtain the collisional ionization data with/without excitation autoionization. At given electron temperatures and densities, a stiffness **A** matrix will be constructed by a set of coupled linear equations, that is $\mathbf{A}\vec{N} = 0$ with initial conditions of $\vec{N}_0 = \{1, 0, 0, \dots, 0\}$. Iterative biconjugate gradient and Gaussian elimination methods from the available IDL library (linbcg.pro and invert.pro) are adopted to solve these equations and obtain the resultant population of the level and the line emissivity ($\epsilon_{ij} = A_{ij}N_j$). By selecting appropriate line profiles with a given line width, a spectrum at a given temperature and density pair will be presented in an editable wavelength range at the bottom of the graphical ECPTTE module. Here only the Gaussian profile is implemented. One feature of the ECPTTE module is that the electron density is a slider widget. Calculations for the whole range of electron density will be done immediately. Users do not need to rerun the code when they change the electron density. By only sliding the pointer to different values within a given density range users can interactively plot the spectra.

For He-like ions, the module of satellite lines due to the dielectronic recombination process is implemented by using the following formula:

$$I_s^{\text{DR}} = 4\pi^{3/2}a_0^{3/2}X_{\text{He}}n_eT_e^{-3/2}\exp\left(\frac{-E_s}{kT_e}\right)g_sA^rB^a, \quad (9)$$

where X_{He} is the ionic fraction of He-like ions in equilibrium and/or non-equilibrium, B^a is the total autoionization branching ratio $\frac{\sum A^a}{\sum A^a + \sum A^r}$, A^r is the radiative decay rate, a_0 is the Bohr radius, T_e is the plasma temperature, and E_s and g_s are the energy and upper level of the satellite transition, respectively.

The module (ECP-EBIT) that is used for spectroscopic modeling of plasma from the EBIT is presented in Figure 3b. The scheme is basically the same as the ECPTTE module for thermal electrons. The available DR and RR rates are for thermal electrons, so no DR or RR contributions to the population of a level are implemented in this module.

The principle of EBIT is that a directional electron beam is compressed by a strong magnetic field, which then ionizes molecular mixtures or gases at the center of the trap. The compressed electrons will generate a negative charge potential. Separate widgets to describe the EBIT conditions are setup for the calculation of the space charge potential. The ‘Dependence’ block determines the calculation to be done as a function of the beam energies or electron densities. The ranges of beam energy and electron density are controlled by two slider widgets. Additionally, the directional electrons will generate anisotropic line emissions. A button is implemented to select and input the available polarization data. Another important feature is the treatment of de-excitation rates. For thermal electrons, a detailed balance principle is used to derive the de-excitation rates from the excitation rates, $q_{ji} = q_{ij}\frac{g_i}{g_j}e^{E_{ij}/kT_e}$, where $E_i < E_j$. But for non-thermal electrons, the detailed balance principle for excitation rates will not be valid. However, the basic atomic process is still reversible, and the relation between excitation cross section (σ_{ij}) and de-excitation cross section (σ_{ji}) holds for nonthermal electrons, that is $g_iE_i\sigma_{ij} = g_jE_j\sigma_{ji}$.

Figure 4 shows the comparison of iron spectra between the thermal electrons and monoenergetic beam along with the measurement of EBIT at a beam energy of 5.64 keV made in Heidelberg (Liang et al. 2009). Gillaspay et al. (2011) reported that the non-consistency of the measured $3C/3D$ ratio

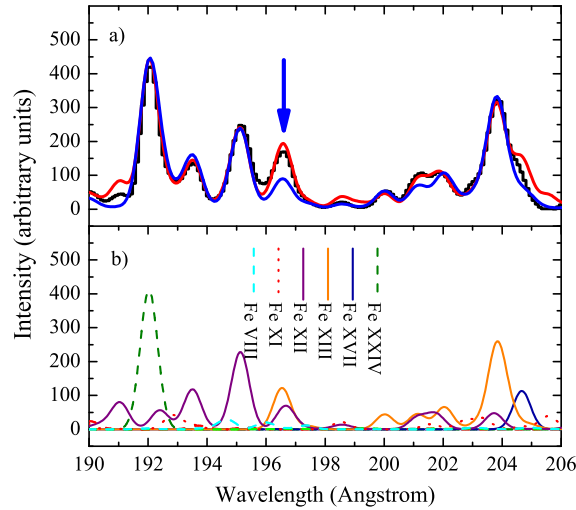


Fig. 4 (a) Simulated spectra with thermal (thick red line, at $n_e = 5.0 \times 10^{10} \text{ cm}^{-3}$ and $T_e = 10^7 \text{ K}$) and monoenergetic beam (thick blue line, at electron energy of 5.64 keV) along with the EBIT measurement (made in Heidelberg, Liang et al. 2009) in the wavelength range from 190 Å to 206 Å. (b) Contributions from Fe VIII to Fe XXIV are shown by different colored curves. The blue arrow denotes that the line emissivity at 196.6 Å is significantly affected by non-thermal electrons.

at the EBIT facility is due to the resonant contribution near the threshold region. So, we set the original collision strength to be an input parameter, not the scaled effective collision strength as was done in Chianti (Landi et al. 2012). Excitation data calculated with the *R*-matrix are not feasible for distribution, so we use the offline data but provide a code (Gaussian averaging) for online access to the original collision strength.

3.2 ECTP Module for Non-equilibrium Collisional Plasma

Some literatures have attributed discrepancies between observations and theories to be the equilibrium adopted (Milligan 2011), especially during sudden events related to solar activities, such as the impulsive phase of flares, the acceleration phase of coronal mass ejections and solar winds (Landi et al. 2012b). So, we set up the ECTP module for non-equilibrium spectroscopy. The flowchart for this module is the same as that in Figure 3 except for the solver block ($d\vec{N}/dt \neq 0$) as well as some technical parameters (see Fig. 5 for the interface). Online data calculations have also been implemented by using Breit-Pauli AUTOSTRUCTURE and FAC methods. Here we adopt the IDL code LSODE to numerically solve the set of stiff ordinary differential equations. One important technique that is different from the equilibrium cases discussed in the previous section is that the charge state distribution is also non-equilibrium when selecting the DR, RR and CI processes. Here, for illustration, the non-equilibrium charge state distribution (\vec{Q}) will be done implicitly with the initial condition $\vec{Q}_0 = \{1, 0, 0, \dots, 0\}$.

Figure 6 shows the relative level of the population for the Si X ion at an electron density of 10^{10} cm^{-3} and an electron beam energy of 500 eV, with its spectra at different times during the evolution. This demonstrates that the dynamics of the population will achieve equilibrium at an ionization parameter of $\sim n_e t = 1.2 \times 10^9 \text{ cm}^{-3} \text{ s}$, which indicates that a non-equilibrium phenomenon in spectroscopy can be detected in low-density astrophysical plasmas. With this ionization param-

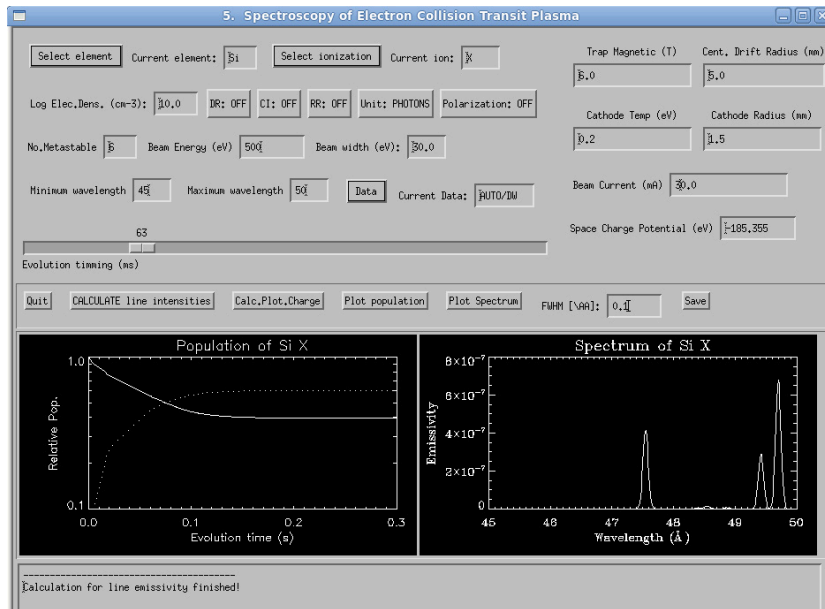


Fig. 5 The interface of the ECTP module for electron collisional transit plasma.

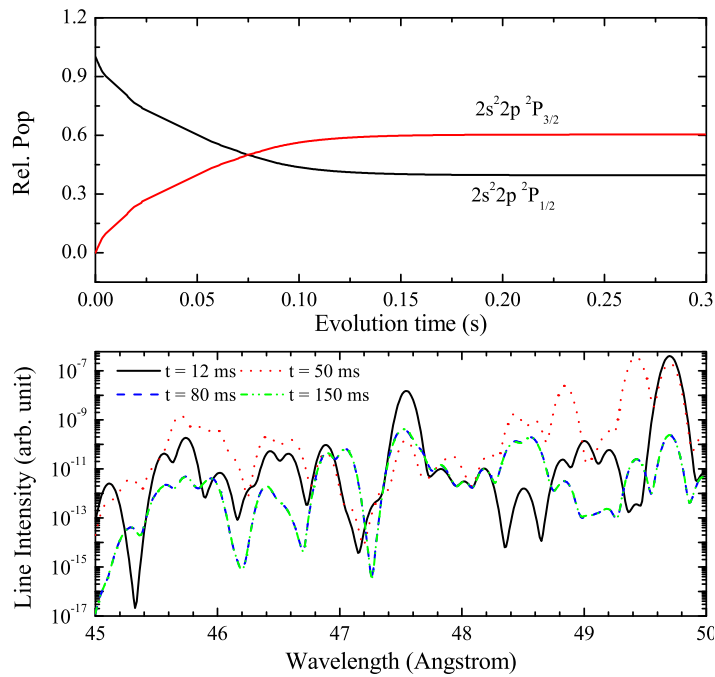


Fig. 6 Upper panel: Time evolution of relative population of Si X at an electron density of 10^{10} cm^{-3} and a beam energy of 500 eV. Bottom panel: Corresponding soft X-ray spectra within the wavelength range of 45–50Å at different times of $t = 12, 50, 80$ and 150 ms.

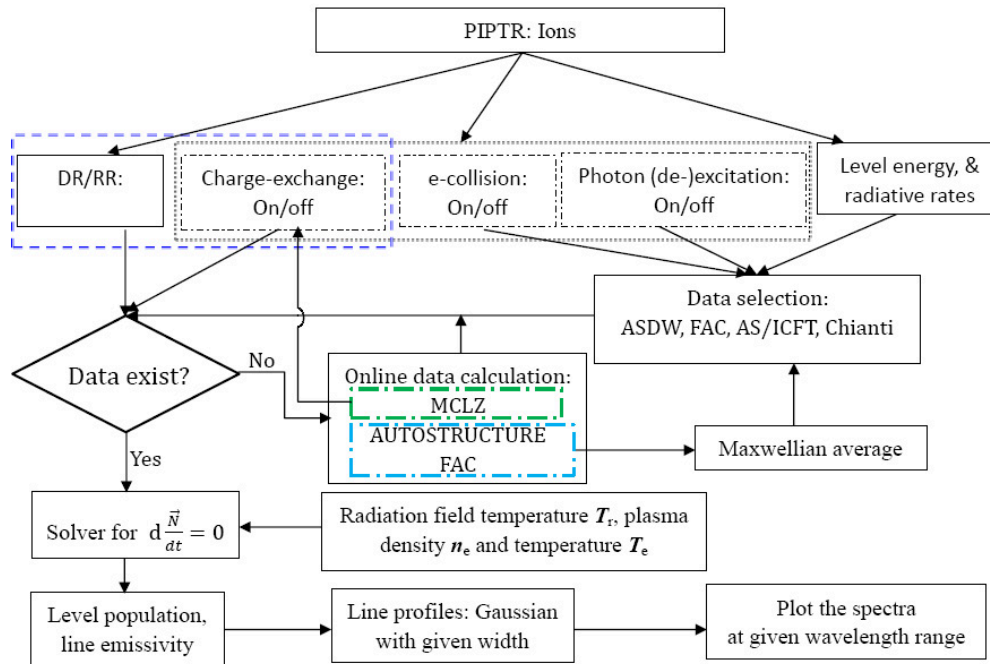


Fig. 7 Flowchart of the PIPTR module for the spectroscopy of photoionization plasma. Online calculations for energy levels, radiative decay rates and electron impact excitations by using AUTOSTRUCTURE and FAC codes have been implemented. Moreover, online calculation is performed for the charge-exchange cross section by using the multi-channel Landau-Zenner approximation. Dotted-boxes denote processes to be selected. The dashed blue box corresponds to atomic data that are compiled from the literature or public websites (*see online version*). The dash-dotted green and blue boxes separate the online calculation for charge-exchange (MCLZ) from structure calculation (ASDW, FAC etc), i.e. energy level, and radiative decay rates.

eter, the soft X-ray spectra show different behaviors at different evolution times of 12, 50, 80 and 150 ms. Some emission lines are strengthened, while some lines are weakened with time evolution.

3.3 PIPTR Module for Photoionized Plasma

Figure 7 shows the flowchart of the PIPTR module for spectroscopy of the photoionized plasma. In this module, energy levels, radiative decay rates and level-resolved DR/RR rates are necessary atomic processes as marked by solid boxes in the top part of this figure. Partial level-resolved DR, RR and photoionization rates⁵ from the series of works (Badnell 2003, 2006) are stored in the present SASAL database in ADAS⁶ format –adf09, adf48 and adf39, respectively. Automatic level matching procedures are developed to read these files and to match the present database with online calculations for energy levels and radiative decay rates. As an explanation for the collisional modules, the dotted boxes correspond to these optional atomic processes, while the dashed boxes refer to data that are compiled from published papers and public websites. For the charge-exchange cross section, online calculation based on the selected energy levels can be done by using the multi-channel Landau-Zener approximation in addition to compilation from published papers. If the electron col-

⁶ www.adas.ac.uk

lision process is selected, the plasma temperature and electron density also need to be set as input parameters in addition to the temperature of the radiation field. Here, the black body radiation source is assumed in the present version. The module for plasmas radiated by the advanced light source (i.e. free-electron lasers) is in the design, as marked in Figure 1 by the block without a color background in the photoionization module.

Radiative recombination continuum (RRC) is an important feature in high-resolution spectroscopy of photoionized winds, i.e. Cygnus X-3 (Paerels et al. 2000), so we implemented such emissions into this module. The RRC emissivity by this process is given as (Tucker & Gould 1966),

$$\frac{E}{dtdVd\omega} = \frac{dP}{dVdE_\gamma} = n_e n^{(q+1)+} E_\gamma \sigma^{\text{rec}}(E_e) v_e \frac{f(v_e) dv_e}{dE_\gamma}, \quad (10)$$

where E_γ is the photon energy of recombination radiation, σ^{rec} is the recombination cross section, and $f(v_e)$ denotes the distribution of electron velocity in a plasma. By the Milne relation between photoionization (σ^{PI}) and recombination cross section (Raymond & Smith 1977), as well as the Maxwell-Boltzman distribution $f(v_e)$ for electron velocities, the above equation can be written as

$$\frac{dP}{dVdE_\gamma} = \frac{4\pi}{c^2} (2\pi m_e k T_e)^{-3/2} n_e n^{(q+1)+} E_\gamma^3 \frac{g^{q+}}{g^{(q+1)+}} \exp\left(-\frac{E_\gamma - I^{q+}}{k T_e}\right) \sigma^{\text{PI}, q+}(E_\gamma), \quad (11)$$

where g^{q+} is the statistical weight of a $q+$ charged ion. By fitting the RRC features in observations, the temperature of radiated absorbers can be estimated as done by Paerels et al. (2000) for the photoionized wind in Cygnus X-3.

Figure 8 shows the resultant spectra for helium-like oxygen with a black body radiation field of 20 eV. Moreover, the effects from electron impact excitation and photon excitation are investigated. Here, photoionization and dielectronic and radiative recombination processes are necessary in this module, as mentioned above. When the photon excitation and de-excitation with dilution factor (namely, $\varphi = 0.5[1 - \sqrt{1 - 1/r^2}]$, where $r = d/R_*$ is the ratio between the distance d of an irradiated medium to the radiation source and the radius of the radiation source R_*) of $\varphi = 10^{-5}$ are further taken into account, the intercombination line 21.8 Å is increased, but the forbidden transition at 22.10 Å is decreased. The electron impact (de-)excitation is found to have the same effect on strengthening the intercombination line, but its contribution is weaker than photon (de-)excitation.

3.4 CXPTE Module for Charge-exchange Plasma

The charge-exchange mechanism is regarded as a popular explanation for X-ray emissions in geocoronal plasmas, i.e. cometary objects, planetary exospheres (Lisse et al. 2001; Häberli et al. 1997), contributions in some starburst galaxies and the diffuse X-ray background emissions from the solar system that were reported (Liu et al. 2011; Snowden 2009; Snowden et al. 2009). So, we setup the CXPTE module for spectroscopy of this kind of X-ray emission in astrophysical and laboratory plasmas.

Figure 9 shows the flowchart of this graphical interface for charge-exchange spectroscopy. Because accurate values for charge-exchange cross section are very scarce, we provide a simple online calculation by using the parameterized MCLZRC approximation in addition to data compiled from published papers. In these parameterized MCLZRC online calculations, the target energy levels are from the SASAL database or online AUTOSTRUCTURE and FAC calculations. Additionally, the hydrogenic model adopted by Wegmann (1998) is setup implicitly for comparison or gives an emergent application when there are no CX data available. In this module, multiple target materials (i.e. H, He, H₂, CO, CO₂, CH₄ and H₂O) are setup for extensive application even though there are no accurate CX data available except for the online MCLZRC calculation. Users can directly input their own CX data directly into the SASAL database with a filename like 'c_6.h2o.cx' to perform a specified analysis.

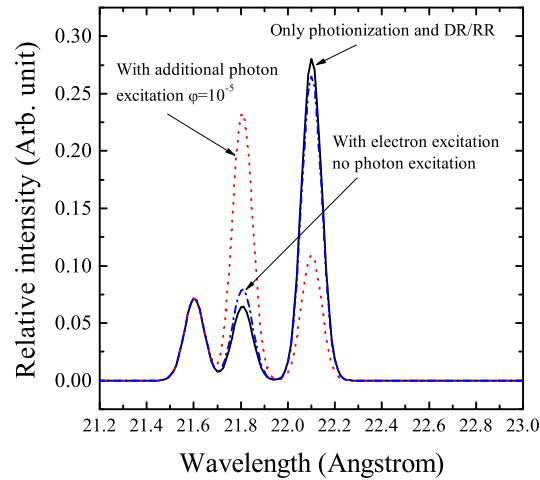


Fig. 8 The spectra of a helium-like oxygen ion (O VII) with black body radiation source $T_r = 20$ eV (solid curves) and electron density of 10^{10} cm^{-3} . The temperature of irradiated plasma is assumed to be 5.0 eV. The blue dash-dotted curve is the spectrum with electron impact (de-)excitation taken into account without photon (de-)excitation (*see online version*). The red dotted curve corresponds to the spectrum with additional photon (de-)excitation, where the dilution factor is 10^{-5} .

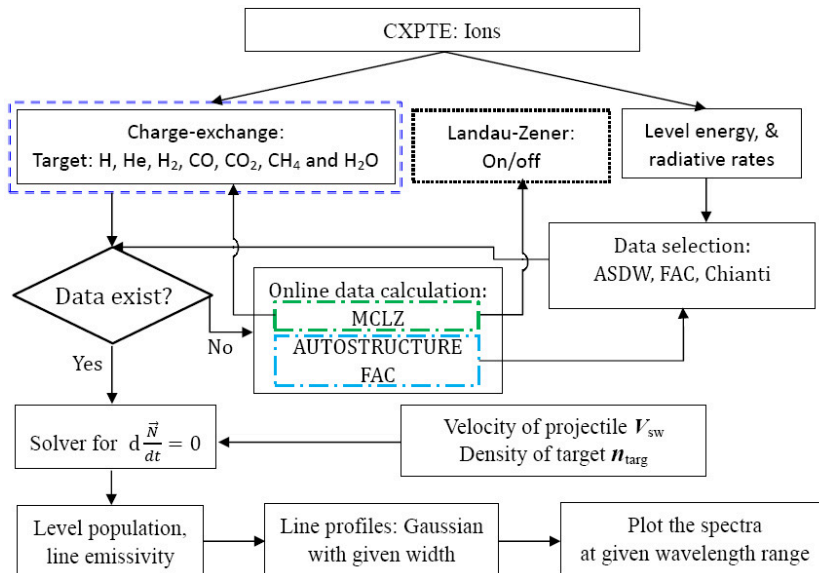


Fig. 9 Flowchart of CXPTE module for the spectroscopy of solar wind ions interacting with planetary exospheres by the charge exchange mechanism. Online calculations for energy levels and radiative decay rates by using AUTOSTRUCTURE and FAC codes have been implemented if no target atomic parameters are available in the SASAL database, which provides the necessary input parameters for online CX cross section calculation by using the parameterized multi-channel Landau-Zenner approximation. This figure uses the same definition for dotted and dashed blue boxes as in Figs. 3 and 7 as well as the same definition of blue and green dash-dotted boxes (*see online version*).

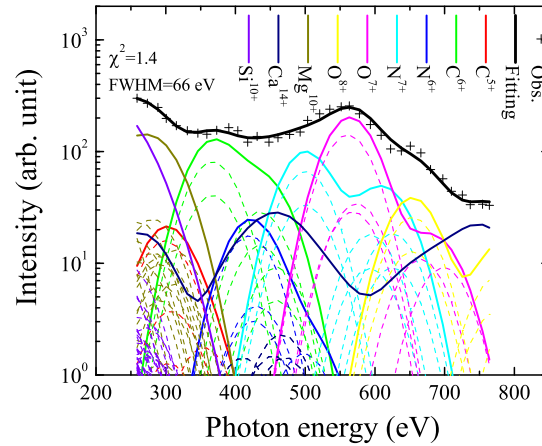


Fig. 10 Calculated X-ray spectra fitted for Linear C/1999 S4 at a solar wind velocity of 600 km s^{-1} . Please see the text for details.

Figure 10 illustrates an example of the CXPT module. By fitting the Chandra observation for Linear C/1999 with simulated CX, solar wind velocity can be derived by setting it to be a free quantity with multiple simulated spectra spanning a large range of solar wind velocities. Here, it is estimated by a test value of 600 km s^{-1} showing an excellent fitting with $\chi^2 = 1.4$ and having good agreement with measurement of 594 km s^{-1} by the space mission *Advanced Composition Explorer* (ACE). Additionally, the composition of solar winds can be estimated by this fitting, which reveals a relative consistency with the previous theories and ACE-data.

3.5 A Module for Charge State Distribution

The charge state distribution and its evolution in plasma is fundamentally important for any study of stellar atmospheres and solar wind. The CHG_BAL module helps us in this analysis for the former two cases in collisional plasma and photoionized plasma, as well as charge-exchange plasma in equilibrium and non-equilibrium, see Figure 11. Since online calculation for collisional ionization has been implemented for ionization cross section in addition to the Chianti (v7, Landi et al. 2012) compilation and Lotz formula — $\sigma = \sum_{i=1}^N \zeta_i \frac{4.5 \times 10^{-14} \ln(E/\chi_i)}{\chi_i E}$, where ζ_i and χ_i are the equivalent electron and ionization potential of the i^{th} -shell, respectively (Lotz 1967), this module can be applied to other nonthermal plasmas with specified distributions. For the dielectronic- and radiative-recombination cases, as well as photoionization, the data are compiled from published papers (Badnell et al. 2003; Badnell 2006; Witthoef et al. 2009, 2011a,b; Nahar et al. 2000) and public websites^{6,5,4}. Three-body and charge transfer recombination processes have been incorporated into the present module. Here, the online hydrogenic CX calculation will be done implicitly to obtain the charge transfer cross section. As done in the previous subsection, an IDL library (linbcg.pro, invert.pro, lsode.pro) will be used to solve the stiff linear and ordinary differential equations. Another important feature is that this module can investigate the metastable contribution of the ionic fraction and its evolution when level-resolved ionization and recombination rates are available.

Figure 12 shows the ionic fraction of ions for thermal and photoionized non-equilibrium plasmas with an initial condition of neutral iron from using this module. For thermal plasma, the plasma condition is set to have typical values of a solar flare, i.e. electron density $n_e = 10^{12} \text{ cm}^{-3}$ and electron temperature $T_e = 500 \text{ eV}$. At a timescale when $n_e t = 2.0 \times 10^{11} \text{ cm}^{-3} \text{ s}$, the plasma achieves equi-

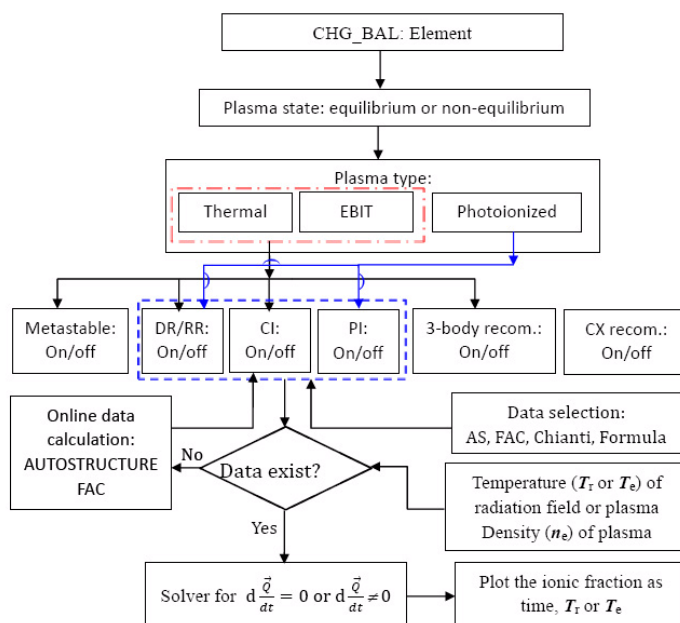


Fig. 11 Flowchart of the CHG_BAL module for charge state distribution in collisional (e.g. thermal and monoenergetic electrons) and photoionized plasmas in equilibrium and non-equilibrium. The collisional ionization can be obtained by online calculation with AUTOSTRUCTURE and FAC methods. This figure uses the same definition for the dashed-blue box as in Figs. 3 and 7. The dash-dotted box represents plasma heated by collisions of electrons.

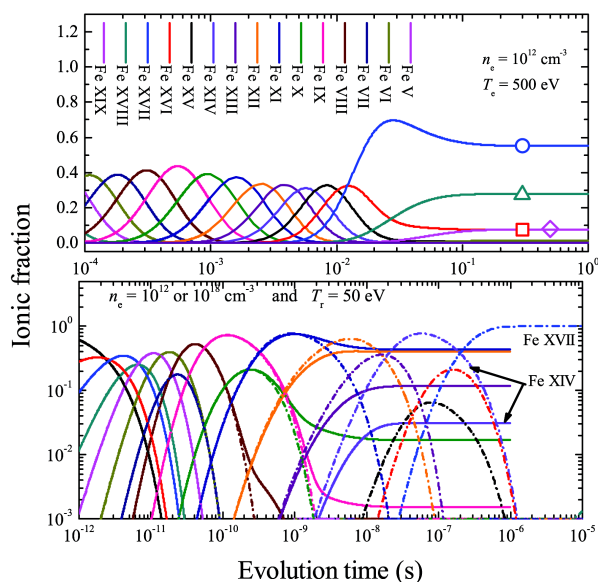


Fig. 12 The charge state distribution of iron ions as a function of the evolution time with the initial neutral iron in collisional and photoionized plasmas. *Top*: For thermal plasma with solar flare conditions, i.e. electron density of $n_e = 10^{12} \text{ cm}^{-3}$ and electron temperature of $T_e = 500 \text{ eV}$. The symbols are from the ionization equilibrium of Bryans et al. (2009). *Bottom*: for photoionized plasma with density of 10^{12} cm^{-3} (dash-dotted line) and 10^{18} cm^{-3} (solid line), and a radiation temperature $T_r = 50 \text{ eV}$ for both densities.

librium and shows good agreement with previous equilibrium values (Bryans et al. 2009). Moreover, the charge state distribution takes a longer time than level dynamics by about two orders of magnitude that are mentioned above for Si X ion. For photoionized plasma, coronal density (10^{12} cm^{-3}) and high density (10^{18} cm^{-3}) in plasma produced by a laser with the same radiation temperature of $T_r = 50 \text{ eV}$ were selected for comparison. This indicates that the electron density will shorten the timescale to achieve equilibrium to tens of nanoseconds. However, it will decrease the measurable ($f_q \geq 0.001$, where f_q is a fraction of the q -charged ion) maximum charge state, for example, Fe XVII is the highest charge state at coronal density, and it will be Fe XIV at high density.

4 SUMMARY AND CONCLUSIONS

In this work, we present a detailed description of the SASAL package for X-ray and EUV spectroscopy for coronal-like, photoionized and geocoronal plasmas, as well as their charge state distribution. The whole package is separated into two parts for equilibrium and non-equilibrium plasmas. For electron collision plasmas, ECPTE and ECP_EBIT modules can be used for thermal electrons and a monoenergetic beam with Gaussian expansion, respectively. The ECTP module benefits from spectroscopic modeling for collisional non-equilibrium plasmas. For photoionized plasmas, the PIPTR module collects a lot of accurate dielectronic- and radiative recombination data, as well as photoionization data from the atomic physics community, which are more applicable than models with data from empirical formulas. A graphical charge-exchange module of CXPTTE significantly improves the spectral analysis for cometary objects and planetary exospheres in X-ray and EUV regions, due to its online CX calculation and the scarcity of available values for CX cross section. Moreover, we setup a CHG_BAL module for the analysis of the charge state distribution in equilibrium and non-equilibrium plasmas dominated by electron collision, photoionization and charge-exchange processes separately, or as a hybrid. In conclusion, the SASAL package will significantly benefit the laboratory astrophysics community in spectroscopy, and further the understanding of radiative loss and heating mechanisms of X-ray emitters in the Universe.

Acknowledgements This work was supported by the National Basic Research Program of China (973 Program) under grant 2013CBA01503, and by the One-Hundred-Talents program of the Chinese Academy of Sciences (CAS). We also acknowledge the support from the National Natural Science Foundation of China (Grant Nos. 11273032, 11273033, 11390371, 11205015, 11173032 and 11135012). J.Y.Z. also acknowledges the Beijing Nova Program (Z131109000413050).

References

- Ashton, C. E. 1993, A Study of Warm Absorbers in Active Galactic Nuclei, Ph.D. thesis, University of London
Badnell, N. R. 1986, *Journal of Physics B Atomic Molecular Physics*, 19, 3827
Badnell, N. R. 2006, *ApJS*, 167, 334
Badnell, N. R., O'Mullane, M. G., Summers, H. P., et al. 2003, *A&A*, 406, 1151
Beiersdorfer, P., Vogel, D. A., Reed, K. J., et al. 1996, *Phys. Rev. A*, 53, 3974
Beiersdorfer, P., Brown, G., Utter, S., et al. 1999, *Phys. Rev. A*, 60, 4156
Beiersdorfer, P., Boyce, K. R., Brown, G. V., et al. 2003, *Science*, 300, 1558
Bodewits, D., Christian, D. J., Torney, M., et al. 2007, *A&A*, 469, 1183
Bryans, P., Landi, E., & Savin, D. W. 2009, *ApJ*, 691, 1540
Butler, S. E., & Dalgarno, A. 1980, *ApJ*, 241, 838
Ferland, G. J., Korista, K. T., Verner, D. A., et al. 1998, *PASP*, 110, 761
Foord, M. E., Heeter, R. F., van Hoof, P. A., et al. 2004, *Physical Review Letters*, 93, 055002
Fournier, K. B., Finkenthal, M., Pacella, D., et al. 2001, *ApJ*, 550, L117
Fujioka, S., Takabe, H., Yamamoto, N., et al. 2009, *Nature Physics*, 5, 821

- Gao, C., & Zeng, J. 2010, *Phys. Rev. A*, 82, 062515
- Gillaspay, J. D., Lin, T., Tedesco, L., et al. 2011, *ApJ*, 728, 132
- Gu, M. F. 2008, *Canadian Journal of Physics*, 86, 675
- Haberli, R. M., Gombosi, T. I., DeZeeuw, D. L., Combi, M. R., & Powell, K. G. 1997, *Science*, 276, 939
- Janev, R. K., Belic, D. S., & Bransden, B. H. 1983, *Phys. Rev. A*, 28, 1293
- Kallman, T., & Bautista, M. 2001, *ApJS*, 133, 221
- Landi, E., Del Zanna, G., Young, P. R., Dere, K. P., & Mason, H. E. 2012a, *ApJ*, 744, 99
- Landi, E., Gruesbeck, J. R., Lepri, S. T., Zurbuchen, T. H., & Fisk, L. A. 2012b, *ApJ*, 761, 48
- Liang, G. Y., Baumann, T. M., López-Urrutia, J. R. C., et al. 2009, *ApJ*, 696, 2275
- Liang, G. Y., Badnell, N. R., & Zhao, G. 2012, *A&A*, 547, A87
- Liang, G. Y., Li, F., Wang, F. L., et al. 2014, *ApJ*, 783, 124
- Lisse, C. M., Christian, D. J., Dennerl, K., et al. 2001, *Science*, 292, 1343
- Liu, J., Mao, S., & Wang, Q. D. 2011, *MNRAS*, 415, L64
- Lotz, W. 1967, *ApJS*, 14, 207
- Mewe, R., Kaastra, J. S., & Liedahl, D. A. 1995, *Legacy*, 6, 16
- Milligan, R. O. 2011, *ApJ*, 740, 70
- Nahar, S. N., Pradhan, A. K., & Zhang, H. L. 2000, *ApJS*, 131, 375
- Paerels, F., Cottam, J., Sako, M., et al. 2000, *ApJ*, 533, L135
- Raymond, J. C., & Smith, B. W. 1977, *ApJS*, 35, 419
- Smith, R. K., Brickhouse, N. S., Liedahl, D. A., & Raymond, J. C. 2001, *ApJ*, 556, L91
- Smith, R. K., Foster, A. R., & Brickhouse, N. S. 2012, *Astronomische Nachrichten*, 333, 301
- Snowden, S. L. 2009, *Space Sci. Rev.*, 143, 253
- Snowden, S. L., Collier, M. R., Cravens, T., et al. 2009, *ApJ*, 691, 372
- Tucker, W. H., & Gould, R. J. 1966, *ApJ*, 144, 244
- Verner, D. A., Ferland, G. J., Korista, K. T., & Yakovlev, D. G. 1996, *ApJ*, 465, 487
- Wegmann, R., Schmidt, H. U., Lisse, C. M., Dennerl, K., & Englhauser, J. 1998, *Planet. Space Sci.*, 46, 603
- Witthoeft, M. C., Bautista, M. A., Mendoza, C., et al. 2009, *ApJS*, 182, 127
- Witthoeft, M. C., García, J., Kallman, T. R., et al. 2011a, *ApJS*, 192, 7
- Witthoeft, M. C., Bautista, M. A., García, J., et al. 2011b, *ApJS*, 196, 7
- Wu, Y., Stancil, P. C., Liebermann, H. P., et al. 2011, *Phys. Rev. A*, 84, 022711